

Metallurgical study on erosion and corrosion behaviors of steels exposed to liquid lead–bismuth flow

Masatoshi Kondo ^{a,1}, Minoru Takahashi ^{b,*}, Tadashi Suzuki ^b,
Kotaro Ishikawa ^a, Koji Hata ^c, Suizheng Qiu ^d, Hiroshi Sekimoto ^b

^a Department of Nuclear Engineering, Graduate School of Science and Engineering, Tokyo Institute of Technology, 2-12-1 O-okayama, Meguro-ku, Tokyo 152-8550, Japan

^b Research Laboratory for Nuclear Reactors, Tokyo Institute of Technology, 2-12-1 O-okayama, Meguro-ku, Tokyo 152-8550, Japan

^c Nuclear Development Corporation, 622-12 Funaishikawa, Tokai-mura, Ibaraki 319-1111, Japan

^d Department of Nuclear & Thermal Power Engineering, Xi'an Jiaotong University, 710049 Xi'an, PR China

Abstract

The mechanism of erosion and corrosion of steels in lead–bismuth eutectic (45Pb–55Bi) flow was investigated. Nine steels were simultaneously exposed to the Pb–Bi flow at the temperature of 550 °C, the loop temperature difference of 150 °C, and the flow velocity of 2 m/s for 1000 h. The liquid metal corrosion, or Pb–Bi penetration into steels occurred in all the steels, and severe erosion took place in some of the steels under low oxygen concentration of 2×10^{-9} wt% in Pb–Bi. The corrosion layer penetrated by Pb–Bi was deeper in the steels containing a lower content of Cr. It was confirmed that the erosion was caused by hydrodynamic carrying away of weakened surface materials due to Pb–Bi penetration. The large-scale erosion could be caused by the detachment of lumps of corroded materials that had defects formed by dissolution of alloying elements.

© 2005 Elsevier B.V. All rights reserved.

1. Introduction

The compatibility of steels with a liquid lead–bismuth eutectic (45Pb–55Bi) flow is one of the key issues for the development of accelerator driven systems (ADS) with a target of Pb–Bi and Pb–Bi cooled fast breeder reactors (FBRs) [1]. It has been expected to have a corrosion resistance of steels if stable oxide films are formed on

the surface of the steels as protective layers by controlling oxygen potential in the Pb–Bi adequately.

However, it is probable that some of spallation products in the target of the ADS may decrease the oxygen potential in the Pb–Bi to a value less than that necessary for the formation of Fe₃O₄. As a result, iron oxide films covering the steels are reduced, and the steel surface is directly exposed to Pb–Bi flow, which leads to the liquid metal corrosion (LMC) where steel elements dissolve into Pb–Bi. An aluminum coating on the steel surface is expected to be effective for the formation of a protective oxide layer since the aluminum is easily oxidized at low oxygen potentials. However, the effectiveness of the aluminum coating has not been demonstrated yet. If the

* Corresponding author. Tel./fax: +81 3 5734 2957.

E-mail addresses: 04d19069@nr.titech.ac.jp (M. Kondo), mtakahas@nr.titech.ac.jp (M. Takahashi).

¹ Tel./fax: +81 3 5734 2957.

protective oxide layer is not formed successfully, the steel corrosion is not inhibited.

The LMC may accompany Pb–Bi penetration into the steel where mechanical strength may be weakened. As the dynamic pressure and shear stress of the Pb–Bi flow acting on the steel surfaces are ten times as high as those of ordinary fluids such as water because of high density of the Pb–Bi, the mechanically weakened parts may be broken by the fluid-mechanical forces. This type of fluid-mechanical damage is called ‘erosion’. The erosion should be avoided since it causes serious damage of material and a large weight loss. The erosion of steels exposed to a Pb–Bi flow has been reported so far [2,3]. The erosion can be classified to the widely damaged surface along the flow as if fluid carries out the surface material by a strong dynamic pressure and the pitting type erosion where material is deeply lost from narrow surfaces.

Although the apparent feature of the erosion, such as damaged surface shapes, has been reported so far, the mechanism of the erosion has not been made clear yet. In order to know the mechanism, the behavior of the eroded parts must be observed metallurgically. In the present study, the corrosion/erosion test of nine steels in a Pb–Bi flow was carried out at low oxygen potential and high velocity, and the behavior of erosion and that of corrosion around the eroded region was investigated metallurgically.

2. Experimental apparatus and procedure

2.1. Experimental apparatus and conditions

Fig. 1 shows the Pb–Bi forced convection-type corrosion test apparatus [4] used for the corrosion and erosion

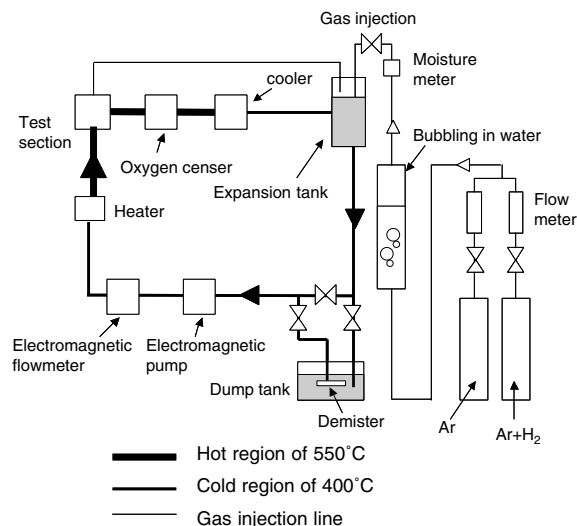


Fig. 1. Lead–bismuth corrosion test loop.

test. The apparatus consists of the electromagnetic pump, the electromagnetic flow meter, the electrical heater, the test section, the air cooler, the expansion tank, and the dump tank. The circulation loop has Pb–Bi inventory of 0.022 m³, and consists of a hot loop region (550 °C) from the heater to the cooler made of STBA26 (9Cr–1Mo steel) to avoid corrosion and a cold loop region (400 °C) made of SS-316. The inside of the test apparatus was heated at 250 °C to achieve clean condition, evacuated and filled with argon having a purity of 99.999% to achieve clean condition. The Pb–Bi was melted in the dump tank at 180 °C for several days. Then, Pb–Bi was charged from the dump tank to the circulation loop which was kept at 250 °C at a flow rate of approximately 0.5 L/min. The Pb–Bi was circulated by the electro-magnetic pump at the rated operation flow rate, and heated up to 400 °C. Then, the electrical heater and air cooler were operated to heat up the Pb–Bi to the temperature of 550 °C, and to cool down Pb–Bi to the temperature of 400 °C, respectively.

Fig. 2 shows a schematic of the test section. A cylindrical test piece holder made of molybdenum was inserted in the test section. Rectangular plate-type test pieces with the thickness of 2 mm and 2.3 mm were mounted in the test piece holder as shown in Fig. 3. The Pb–Bi flows through the two Pb–Bi flow channels above and below the test pieces. The height, width and length of the channels were 2 mm, 13 mm and 425 mm, respectively.

Test conditions are summarized in Table 1.

2.2. Test materials

Alloying components of the test pieces are presented in Table 2. SCM420 is a low alloy steel, STBA28, NF616 and STBA26 have been developed for supercritical pressure boilers, HCM12 and HCM12A are candidates for structural materials of fossil fuel power plants, ODS is a cladding steel strengthened for the use at high temperature and high radiation condition in sodium cooled FBRs, and F82H is foreseen to be used as blanket material in the fusion reactors.

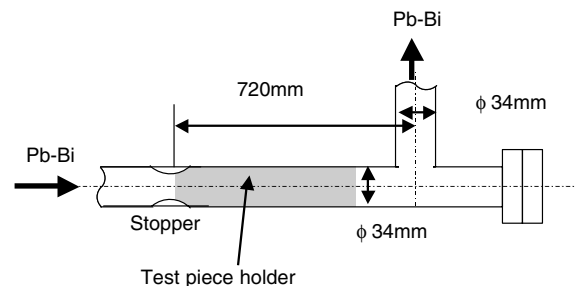


Fig. 2. Schematic of test section.

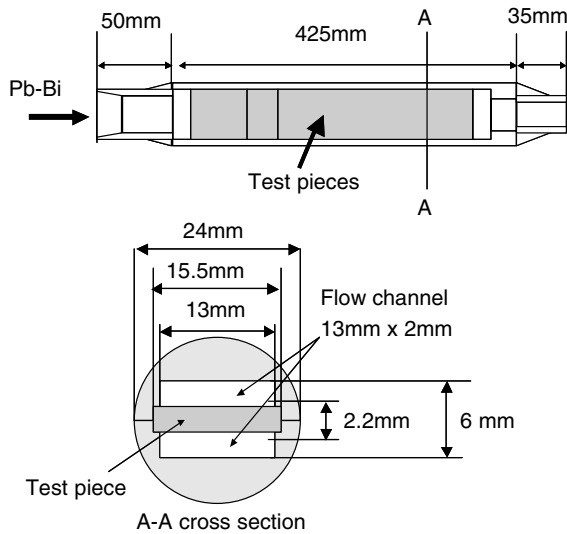


Fig. 3. Schematic of test piece holder.

Table 1

Test conditions

Flow rate (L/min)	6
Flow velocity (m/s)	2
Temperature of hot region (°C) (test temperature)	550
Temperature of cold region (°C)	400
Test time (h)	1000

Table 2

Contents of alloying components in test steels

	Cr	Mo	W	Si	Others
SCM420	1.2	0.2	–	0.2	
F82H	7.7	1.94	1.94	0.1	0.01Ti–0.01Cu
STBA28	8.8	1	–	0.4	
NF616	9	0.5	1.8	0.3	
STBA26	9	1	–	0.2	
ODS	11.7	–	1.9	–	0.29Ti–0.23Y ₂ O ₃ –0.18Y
HCM12A	12	0.3	1.9	0.3	0.9Cu
HCM12	12.1	1.1	1.0	0.3	
SS-316	18	2–3	–	0.1	10–14Ni

The test pieces were mounted in the test piece holder in the following order from upstream to downstream: (1) SCM420, (2) ODS, (3) F82H, (4) STBA26, (5) NF616, (6) HCM12, (7) HCM12A and (8) SS-316.

The test pieces were 15 mm in width, 10 mm in length and 2.3 mm in thickness. In total, four test pieces (a)–(d) of each steel shown in Fig. 4 were exposed to the Pb–Bi flow. The test piece (a) was prepared for metallurgical analysis, the test piece (c) for the measurement of weight

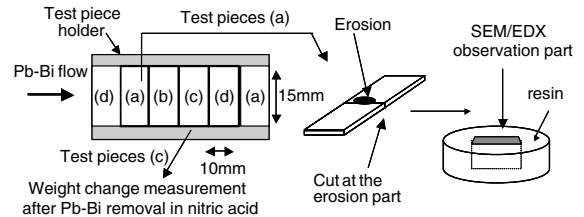


Fig. 4. Test pieces in molybdenum holder and preparation for SEM/EDX observation and analysis.

change, and the test pieces (b) and (d) were spares of (a) and (c).

2.3. Measurement and control of oxygen potential in Pb–Bi

The oxygen sensor was mounted downstream from the test section as shown in Fig. 1 in order to measure oxygen potential in the Pb–Bi flow [2]. The sensor was made of a cylindrical solid electrolyte conductor, ZrO₂–Y₂O₃ with the reference electrode of platinum pasted inner surface in a purged air flow inside the cylinder. The sensor was located in an argon cover gas space, and the Pb–Bi level was increased to contact the sensor with Pb–Bi by depressurizing cover gas in the vessel of the oxygen meter under a constant cover gas pressure in the expansion tank.

In order to control the oxygen potential in Pb–Bi, the steam-moistured argon containing hydrogen was injected into the Pb–Bi flow in the expansion tank at the temperature of 400 °C as shown in Fig. 1 [2]. The injected gas mixture was made by mixing hydrogen and argon and then bubbling them through a water bath. The hydrogen and argon flow rates were measured with purge meters, and the moistured steam concentration was measured by moisture meter and found to be 93%. The partial pressure ratio of hydrogen to steam was estimated from the saturation pressure of the steam at the temperature in the water bath and argon and hydrogen flow rates. The gas mixture heated up in the stainless steel tube was injected in the Pb–Bi as bubbles the expansion tank at the mixture gas flow rate of 70–100 ml/min. The mixture gas remained as a cover gas in the expansion tank for a while, and then flowed out of the tank.

In the present study, the formation of protective oxide layer as described in Refs. [5–7] on the steel surface was inhibited to investigate the erosion and corrosion behaviors in the Pb–Bi with low oxygen content. Fig. 5 shows the diagram of the Gibbs free energy of oxide formation and oxygen potential. If the oxygen concentration of Pb–Bi is kept to be lower than the potential for Fe₃O₄ formation, the steel may have no protective outer oxide films of Fe₃O₄ and no internal

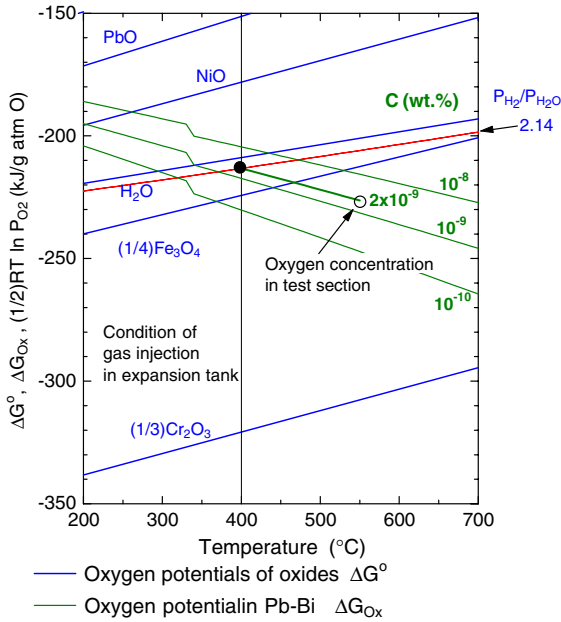


Fig. 5. Diagram of oxygen potential.

layer of $(\text{Fe}, \text{Cr})_3\text{O}_4$. The oxygen potential in Pb–Bi: $(RT/2)\ln P_{\text{O}_2}$ is given by ΔG_{O_x}

$$\Delta G_{\text{O}_x} = \Delta G_{\text{PbO}}^0 + RT \ln \left(\frac{C}{C_s} \right), \quad (1)$$

$$\begin{aligned} \frac{RT}{2} \ln P_{\text{O}_2} &= \Delta G_{\text{PbO}}^0 + RT \ln \left(\frac{C}{C_s} \right) \\ &= \Delta G_{\text{H}_2\text{O}}^0 - RT \ln \left(\frac{P_{\text{H}_2}}{P_{\text{H}_2\text{O}}} \right), \end{aligned} \quad (2)$$

where ΔG_{PbO}^0 is the oxygen potential for formation of PbO which may be firstly precipitated in the oxygen saturated state of Pb–Bi [8]. C is the oxygen concentration in the Pb–Bi, and the saturated concentration or the solubility of oxygen in Pb–Bi at the temperature of T in the unit of wt%, C_s is provided by [9]

$$\log C_s = 1.2 - 3400/T \quad (673 \text{ K} < T < 973 \text{ K}). \quad (3)$$

The curves of constant oxygen concentration and constant partial pressure ratio of H_2 to H_2O are shown in Fig. 5. The partial pressure ratio of $P_{\text{H}_2}/P_{\text{H}_2\text{O}}$ in the gas mixture was chosen to be 2.14. From the value of $P_{\text{H}_2}/P_{\text{H}_2\text{O}}$ in the injected gas, the oxygen potential and the oxygen concentration in the expansion tank was determined from Eqs. (1) and (2). Although the oxygen potential decreases with increasing temperature when Pb–Bi flowed from the expansion tank to the test section, the oxygen concentration in the Pb–Bi may be kept nearly constant as indicated by the thick curve in Fig. 5. Therefore, the oxygen concentration in the test section

was estimated to be 2×10^{-9} wt%; at 550 °C, where Cr_2O_3 might be formed stably but Fe oxide might not be formed because of low oxygen potential.

During the corrosion/erosion test, the oxygen concentration downstream from the test section was measured using the oxygen sensor. It was confirmed that the electromotive force of the oxygen sensor reached an equilibrium value after 80-h gas injection.

2.4. Measurement of weight change and SEM/EDX observation and analysis

After the exposure to the Pb–Bi flow for 1000 h, the test piece holder was immersed in a glycerin pool at temperature of 200 °C to remove adhered Pb–Bi on the test piece surfaces [6,7] and to observe the occurrence of the LMC. The surface of the steels had a metallic luster before the exposure to the Pb–Bi. For the test pieces after the exposure, the change of surface color was checked, and the occurrence of erosion and the existence of adhered Pb–Bi were inspected by microscopy.

For the measurement of weight change, Pb–Bi that has metal elements with higher melting point than that of pure Pb–Bi was removed by applying nitric acid to the test pieces (c). An electronic reading balance with the accuracy of 0.1 mg was used for the measurement of weight change.


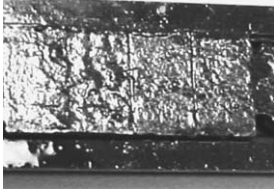
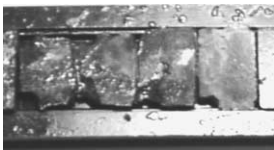






The test pieces (a) were cut across the eroded regions and molded into a resin as shown in Fig. 4. The faces of the cross-section were polished with a mechanical grinder with polishing agent of polycrystalline diamond and lubricant of ethanol, and observed and analyzed using the SEM/EDX.

3. Experimental results

3.1. Surface observation

The photographs of the test piece in the molybdenum holder are shown in Table 3. The surface of SCM420 exhibited severe erosion, particularly on the upstream end of the test piece (a), i.e., the left end of the left test piece shown in Table 3. Dynamic pressure acted there strongly. All of the surface of ODS was covered with Pb–Bi. F82H exhibited severe erosion, particularly at the sides and corners of the test pieces. Although STBA26 exhibited strong erosion, particularly in the test piece (b), no erosion was observed in the test pieces of STBA28 and NF616 in spite that their alloying components were similar to those of STBA26. HCM12 exhibited crack-like erosion, while HCM12A with similar alloying components to those of HCM12 exhibited smooth surface without erosion. The surface of SS-316 was completely covered with Pb–Bi.

Table 3
Photographs of test piece surfaces in molybdenum holder

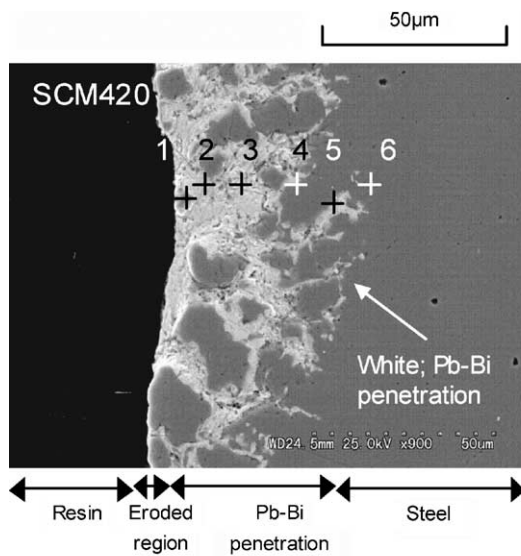
Steel	Surface observation
SCM420 (1Cr) (Erosion)	
ODS (11.7Cr–1.9W– 0.29Ti–23Y ₂ O ₃ –0.18Y) (Covered with Pb–Bi)	
F82H (7.7Cr–1.94Mo– 1.94W–0.01Ti–0.01Cu) (Erosion)	
STBA26 (9Cr–1Mo) (Erosion)	
STBA28 (8.8Cr–1Mo–0.4Si) (Smooth)	
NF616 (9Cr–0.5Mo–8W) (Covered with Pb–Bi)	
HCM12 (12.1Cr–1.1Mo–1.0W) (Erosion)	
HCM12A (12Cr–0.3Mo–9W) (Smooth)	
SS-316 (18Cr–2Mo–12Ni) (Rough surface)	

3.2. SEM/EDX observation and analysis

3.2.1. Corrosion/erosion behaviors in SCM420, ODS and F82H

Fig. 6 shows the results of SEM/EDX observation and analysis for the cross-section of SCM420. A large part of surface material was lost by erosion, and Pb–Bi penetrated into the steel matrix, probably into grain boundaries. The penetration depth was approximately 40 μm. According to EDX analysis, the content of Bi was approximately 80 wt% of metal elements at the positions of No. 2 and 5 in Fig. 6 in the penetration region, and the content of Fe was relatively low, i.e., approximately 10 wt% in the interface between the penetrated region and the steel matrix.

Fig. 7(a) shows the corrosion behavior of ODS in Pb–Bi. It is found that the ODS did not exhibit severe LMC and the Pb–Bi penetration depth was only ≈5 μm. The content of Pb was a little higher than that of Bi in the penetration region, and small amounts of Fe and Cr were detected in the adhered Pb–Bi.



	Point No 1	Point No 2	Point No 3	Point No 4	Point No 5	Point No 6
Fe	72.83	0.23	0.66	99.38	9.88	81.4
Cr	0.37	0	0	0.62	0	0.49
Pb	13.89	8.53	65.26	0	7.69	3.82
Bi	12.9	91.24	33.29	0	82.96	14.32

Unit: wt%

Fig. 6. SEM/EDX observation and analysis for cross-section of eroded region in SCM420.

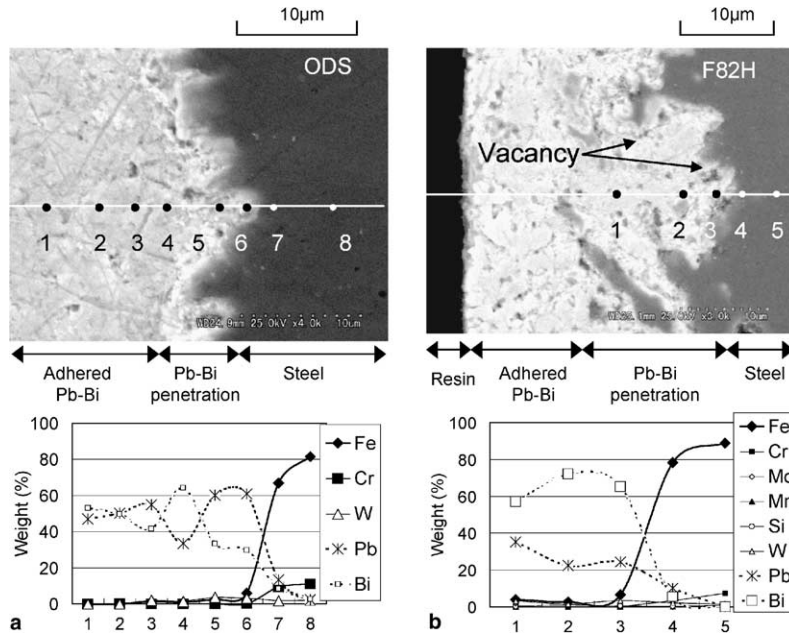


Fig. 7. SEM/EDX observation and analysis for cross-section of corroded region in (a) ODS and (b) F82H.

Fig. 7(b) shows the corrosion behavior of F82H which exhibited Pb–Bi penetration into grain boundary with a depth of up to 22 µm. Some vacancies are observed around the interface between the Pb–Bi penetration region and the steel matrix. The content of Bi was higher than that of Pb in the Pb–Bi penetrated region as it was in SCM420.

Fig. 8(a) and (b) show two types of erosion in F82H, respectively: narrow erosion like pitting and wide erosion. It is found that the pitting was approximately 35 µm in depth and approximately 100 µm in width and Pb–Bi penetrated deeply from the bottom of the pitting. The erosion was approximately 2 mm in width and

200 µm in depth in Fig. 8(b). The enlarged view of the local erosion is shown in Fig. 8(c). It is found that Pb–Bi penetrated so as to envelop a lump of steel, which suggests the mechanism of erosion, that is, the lump of steel may be carried away easily from the steel matrix by the Pb–Bi flow because the strength of the penetration region decreases.

3.2.2. Corrosion/erosion behaviors in STBA26, STBA28 and NF616

Fig. 9(a) shows the corrosion behavior of STBA26. The surface became rough and Pb–Bi penetrated into the steel matrix up to a depth of ≈16 µm. The content

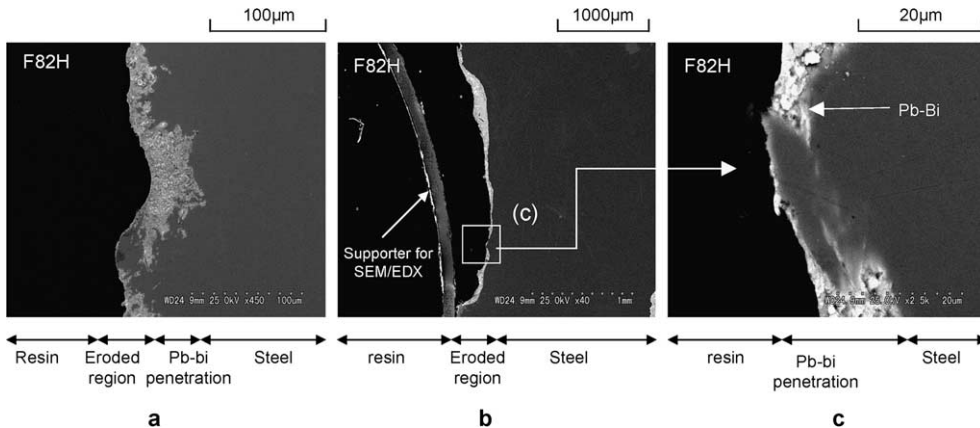


Fig. 8. SEM observation for cross-section of eroded region in F82H: (a) Pb–Bi penetration along narrow erosion, (b) wide erosion and (c) Pb–Bi penetration in widely eroded region.

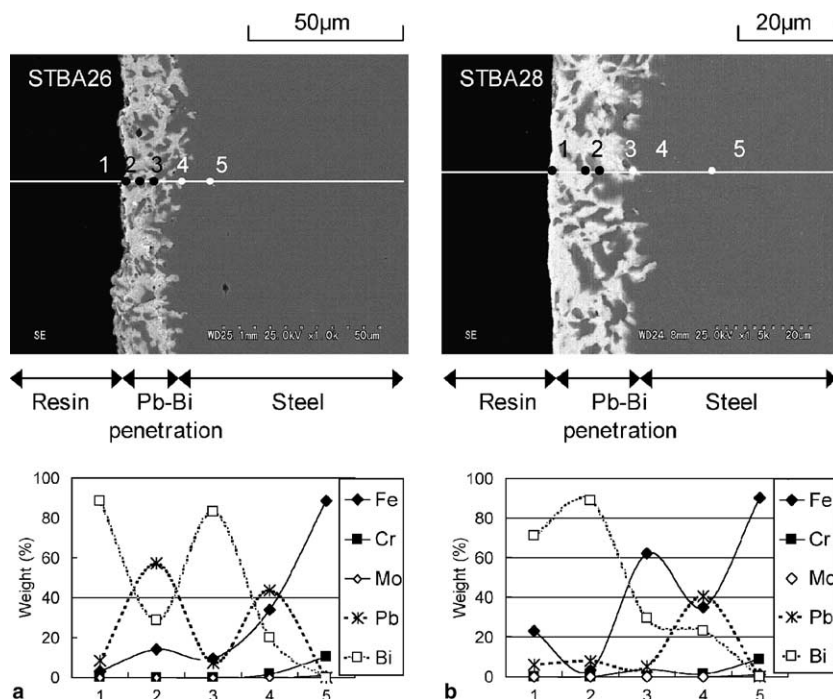


Fig. 9. SEM/EDX observation and analysis for cross-section of corroded region in (a) STBA26 and (b) STBA28.

of Pb was higher than that of Bi near the interface of the penetration region and the steel matrix as shown in the point No. 4 of Fig. 9(a), while Fe was detected in the Pb–Bi penetration region as shown in the point No. 1–3 of Fig. 9(a).

Fig. 9(b) shows the corrosion behavior of STBA28. It exhibited similar corrosion behavior to that of STBA26 possibly because of nearly the same contents of alloying components as those of STBA26. The depth of Pb–Bi penetration was approximately 20 μm . The content of Bi was much higher than that of Pb in the penetration region as indicated by the points No. 1–3 of the EDX analysis in Fig. 9(b), although the content of Pb was approximately 40 wt% in the interface between the penetration region and the steel matrix.

Fig. 10(a) shows the erosion in STBA26 which is 120 μm in depth and 500 μm in width. It is found that Pb–Bi penetrated into the steel matrix, and there appeared some defects in the edge regions shown in Fig. 10(b) and (d). Pb–Bi penetrated more deeply into the steel matrix from the bottom of the eroded region as shown in Fig. 10(c). The result of the EDX analysis in Fig. 10(c) shows that the contents of Pb and Bi were high in the penetration region. The Pb–Bi penetration behavior in the eroded region was similar to that in the corroded region shown in Fig. 10(a).

Fig. 11(a)–(c) show the results of SEM/EDX observation and analysis for cross-sections of NF616. Although erosion in NF616 could not be observed in

the surface observation due to the cover of Pb–Bi, the result of SEM observation indicated the occurrence of erosion in NF616. In the eroded region, some lumps of steel were detached from the surface. Fig. 11(b) shows that Pb penetrated into the steel matrix in the depth of approximately 15 μm from the interface between adhered Pb–Bi and steel matrix. The content of Pb was much higher than that of Bi in the penetrated region as indicated by No. 3–4 in Fig. 11(b). Fig. 11(c) shows the penetration behavior in the corroded region in NF616. It is found that the penetration behavior in the corroded region was similar to that in the eroded region.

3.2.3. Corrosion/erosion behaviors in HCM12 and HCM12A

Fig. 12(a) shows the corrosion behavior of HCM12. The Pb–Bi penetrated into the steel matrix and grain boundary in the depth of approximately 21 μm from a rough interface between steel and adhered Pb–Bi. The content of Pb was higher than that of Bi around the interface as shown in the result of EDX analysis. The adhered Pb–Bi contained Fe and a little amount of Cr. Pb–Bi penetration into grain boundary was observed clearly. Fig. 12(b) shows the Pb–Bi penetration behind some lumps of steel which might be detached easily, and Fig. 12(c) shows the deep Pb–Bi penetration with adhered Pb–Bi in the eroded region. The penetration region was 100 μm deep and 200 μm wide.

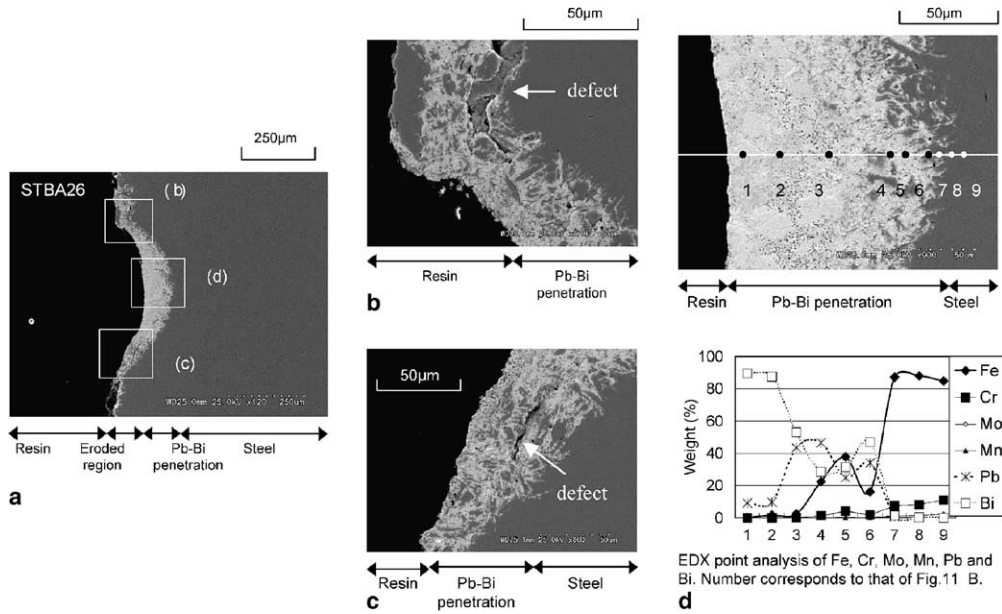


Fig. 10. SEM/EDX observation for cross-section of eroded region in STBA26: (a) erosion, (b,c) end of eroded region, (d) Pb–Bi penetration and EDX analysis.

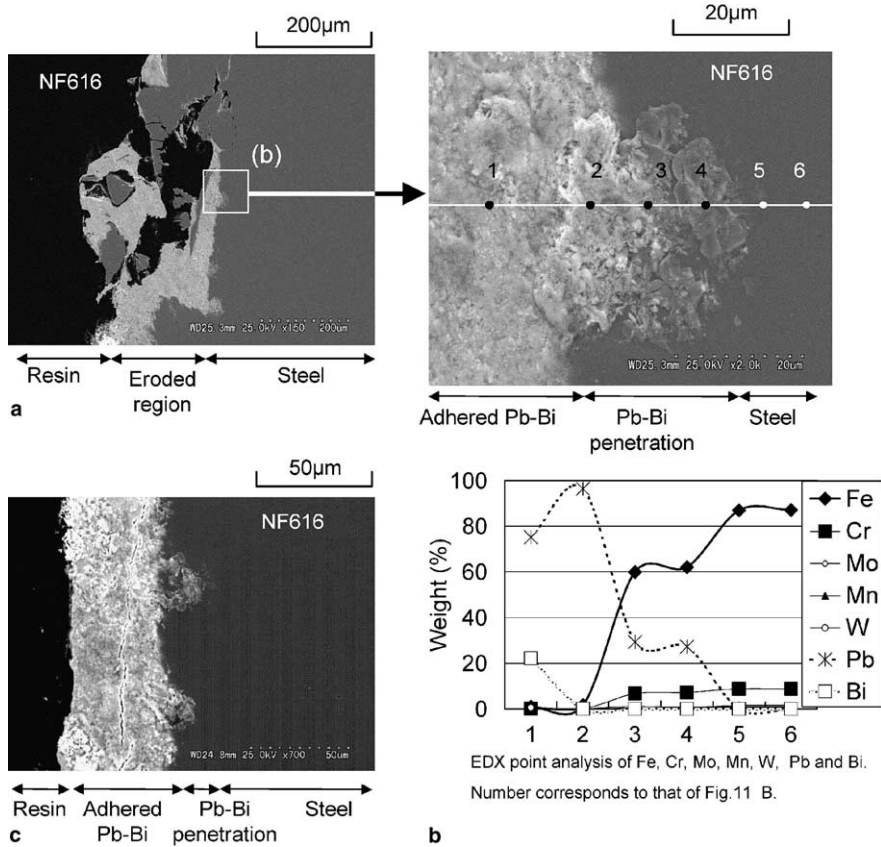


Fig. 11. SEM/EDX observation and analysis in NF616: (a) erosion, (b) Pb–Bi penetration in eroded region and EDX analysis, (c) Pb–Bi penetration in corroded region.

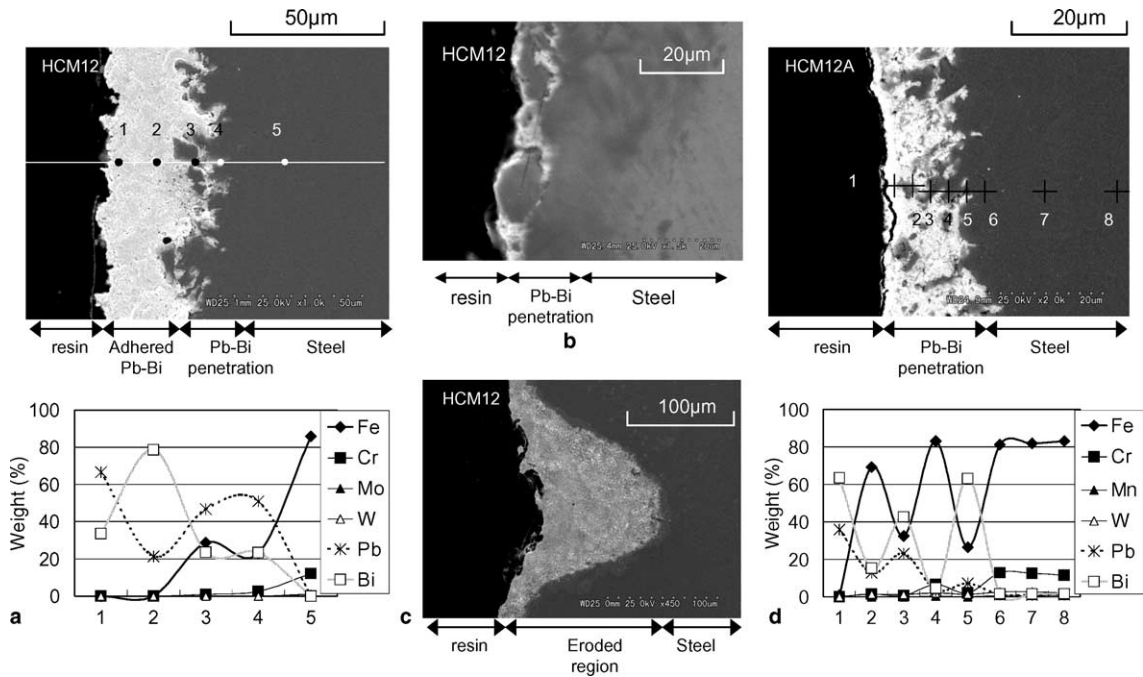


Fig. 12. SEM/EDX observation and analysis for cross-section of HCM12 and HCM12A: (a) corrosion and EDX analysis in HCM12, (b) Pb–Bi penetration in HCM12, (c) erosion in HCM12, (d) corrosion and EDX analysis in HCM12A.

Fig. 12(d) shows the corrosion behavior of HCM12A where Pb–Bi penetrated into a depth of 15 μm . Some continuous holes were observed along the Pb–Bi penetration region. The content of Bi was higher than that of Pb in the Pb–Bi penetration region. There was a little amount of Cr although the content of Fe did not decrease.

and the results of EDX line analysis. Pb penetrated into a depth of approximately 42 μm in the outer region (A), while Pb–Bi penetrated into the depth of 208 μm in the intermediate region (B). The contents of Ni and Cr decreased in the Pb–Bi penetration region, as described in Ref. [4–8].

3.2.4. Corrosion/erosion behaviors in SS-316

SS-316 is corroded up to a depth of $\approx 100 \mu\text{m}$ and erosion has already started (see Fig. 13(a)). The corroded region can be distinguished into two layers from the Pb–Bi penetration behavior into grain-boundaries

4. Weight changes of test pieces

Fig. 14 shows the result of the weight change measurements of the test pieces. The weight loss of SCM420 was the highest, and those of F82H and NF616 were high.

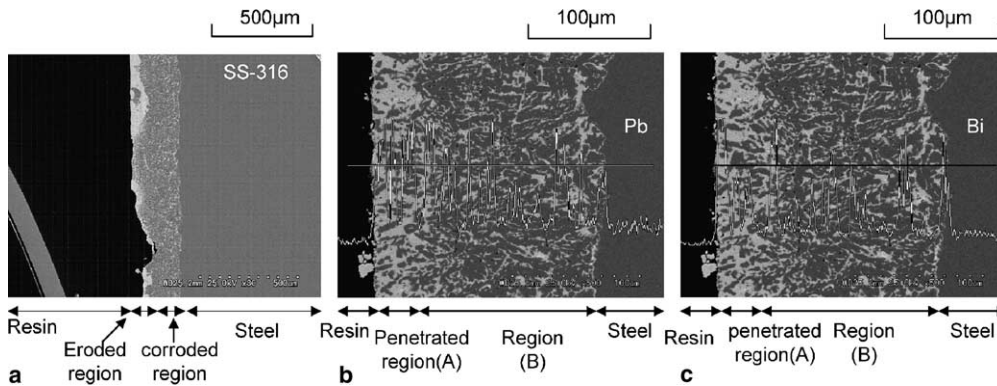


Fig. 13. SEM/EDX observation and analysis for cross-section of eroded region in SS-316: (a) erosion, (b) EDX analysis of Pb content in penetrated region (c) EDX analysis of Bi content in penetrated region.

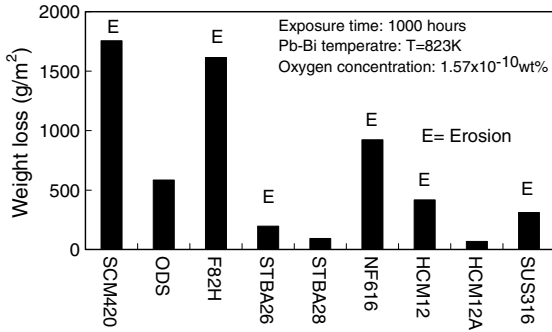


Fig. 14. Weight change of test pieces during 1000-h exposure to Pb–Bi flow.

This is probably because these steels contained low Cr concentration. The weight losses of SCM420, F82H, STBA26, NF616, HCM12 and SUS316 that were eroded were higher than those of ODS, STBA28 and HCM12A that were not eroded. The weight loss of STBA26 was two times as high as that of STBA28, and the weight loss of HCM12 was five times as high as that of HCM12A,

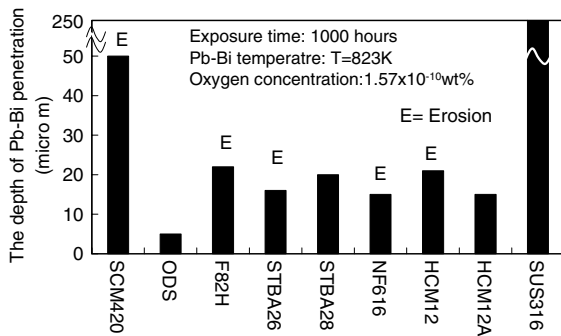


Fig. 15. Depth of Pb–Bi penetration layers in steels.

although the contents of alloying components were nearly as the same as each other in both cases.

5. Discussion

Under the present oxygen potential, the LMC, particularly Pb–Bi penetration, took place in all the steels, and severe erosion occurred in some of the test pieces. In the previous test using Pb–Bi with an oxygen concentration of 5×10^{-7} wt% under comparable test conditions [2,10], LMC and erosion did not occur on the surfaces of the same steels. Therefore, it has been confirmed that oxygen concentration in Pb–Bi lower than the formation potential of Fe_3O_4 suppresses the formation of protective oxide layers and enhances the LMC, and as consequence the erosion as well.

The degree of LMC, or Pb–Bi penetration depth, and erosion may be related to each other, depending on the types of steels: Pb–Bi penetration was deep and erosion occurred in SCM420, F82H and HCM12 as shown in Fig. 15. This may be attributed to low content of Cr, particularly in SCM420 where protective Cr oxide films cannot be formed easily. The corrosion of SS-316 was a special case, that is, it had severe Pb–Bi penetration and erosion although it had high contents of Cr. That is because Ni was dissolved out of the steel surface into Pb–Bi [6,11,12] and a porous layer was formed. The layer was phase-transformed into a ferrite structure where Pb–Bi can easily diffuse. This was demonstrated by the fact that there was no Ni content in the penetration region.

The depth of Pb–Bi penetration was almost the same among STBA26, STBA28 and NF616 possibly because of nearly the same contents of alloying components. The Pb–Bi penetration was not so deep in ODS and HCM12A that had no erosion. In the case of ODS,

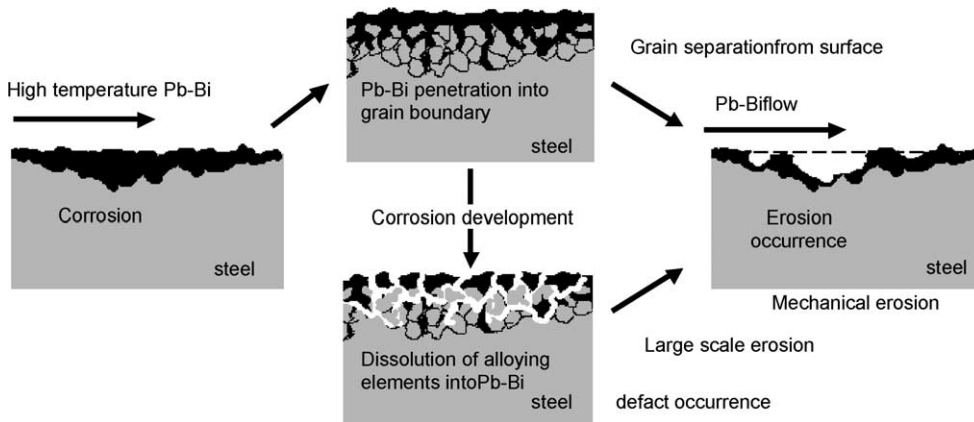


Fig. 16. Schematic of erosion mechanism.

the grain boundary with unique structure [13,14] might beneficially influenced to the erosion.

The process from corrosion to erosion can be explained schematically in Fig. 16. It is described as follows: at first, the LMC occurs on the steel surface exposed to high temperature Pb–Bi, where Pb–Bi penetrates into grain boundaries. The grain boundaries are weakened, and consequently, some grains are taken away from the steel matrix by the hydrodynamic shear forces of the Pb–Bi flow. Some defects formed by dissolution of alloying elements into Pb–Bi may enhance the detachment of a lump of steel from the steel matrix. Therefore, the Pb–Bi penetration might cause large-scale erosion.

6. Conclusion

- (1) Pb–Bi penetration-type corrosion and, in some steels erosion, occurred on the test piece surfaces because no protective oxide layers were formed under the present low oxygen concentration less than the Fe_3O_4 formation potential.
- (2) A relation between liquid metal corrosion (LMC) and erosion has been clarified. The degree of LMC could be evaluated from the depth of the Pb–Bi penetration into steel matrix. The Pb–Bi penetration was deeper in the relatively low Cr steels of SCM420 and F82H than in the high Cr steels: ODS, HCM12, and HCM12A.
- (3) The austenitic steel, SS-316, was a special case where Pb–Bi penetration was deep in spite of high Cr content because of high content of Ni in the steel that dissolves into Pb–Bi and promotes the Pb–Bi penetration. The test steels which were more deeply penetrated by Pb–Bi exhibited more severe erosion.
- (4) Low Cr steel and austenitic steel are more readily eroded under the low oxygen potential.

Acknowledgements

The authors owe experimental assistance to Mr S. Uchida, Mr N. Sawada, Dr S. Yoshida, Mr M. Imai, Dr Y. Yano and Mr A. Yamada, and the measurement assistance of oxygen potential to Mr T. Nishi, Mr K.

Matsuzawa and Mr Umeno. The authors acknowledge the supply of the test material, F82H of Japan Atomic Energy Research Institute (JAERI) and Koukan Keisoku K.K., and the supply of the test material, ODS of Japan Nuclear Cycle Development (JNC). The present study was performed as a part of the Innovative Nuclear Energy System Technology (INEST) Development Projects Adopted in FY2002 (Area of Innovative Nuclear Reactor Technology) supported by the Ministry of Education, Culture, Sports, Science and Technology of Japan.

References

- [1] M. Takahashi, M. Igashira, T. Obara, H. Sekimoto, K. Kikuchi, K. Aoto, T. Kitano, in: Proceedings of the 10th International Conference on Nuclear Engineering (ICONE10), 14–18 April 2002, Arlington, Virginia, USA, ICONE10-22166.
- [2] M. Takahashi, H. Sekimoto, K. Ishikawa, T. Suzuki, K. Hata, S. Que, S. Yoshida, T. Yano, M. Imai, in: Proceedings of the 10th International Conference on Nuclear Engineering (ICONE10), 14–18 April 2002, Arlington, Virginia, USA, ICONE10-22226.
- [3] K. Kamata, T. Kitano, H. Ono, M. Ono, in: Proceedings of the 11th International Conference on Nuclear Engineering (ICONE12), 20–23 April 2003, Tokyo, Japan, ICONE11-36204.
- [4] M. Takahashi, N. Sawada, H. Sekimoto, M. Kotaka, T. Yano, S. Uchida, K. Hata, T. Suzuki, in: Proceedings of the 8th International Conference on Nuclear Engineering (ICONE10), 2–6 April 2000, Baltimore, MD, USA, ICONE8-8507.
- [5] C. Fazio, G. Benamati, C. Martini, G. Palombarini, *J. Nucl. Mater.* 296 (2001) 243.
- [6] G. Benamati, C. Fazio, H. Piankova, A. Rusanov, *J. Nucl. Mater.* 301 (2002) 23.
- [7] F. Barbier, A. Rusanov, *J. Nucl. Mater.* 296 (2001) 231.
- [8] G. Muller, A. Heinzl, G. Schmacher, A. Weisenburger, *J. Nucl. Mater.* 321 (2003) 256.
- [9] B.F. Gromov, Y.I. Orlov, P.N. Martynov, V.A. Gulevsky, in: Proceedings of HLME1999, p. 87.
- [10] M. Takahashi, T. Suzuki, H. Sekimoto, *Trans. Am. Nucl. Soc.* 85 (2001) 300.
- [11] K. Kikuchi, Y. Kurata, S. Saito, M. Futakawa, T. Sasa, H. Oigawa, E. Wakai, K. Miura, *J. Nucl. Mater.* 318 (2003) 348.
- [12] J.R. Weeks, *Nucl. Eng. Des.* 15 (1971) 362.
- [13] S. Ukai, M. Fujiwara, *J. Nucl. Mater.* 307–311 (2002) 749.
- [14] E. Yoshida, S. Kato, *J. Nucl. Mater.* 329–333 (2004) 1393.